

Experimental Assessment of the Performance of High-Frequency CODAR and WERA Radars to Measure Ocean Currents in Partially Ice-Covered Waters

EMNA KAMLI, CÉDRIC CHAVANNE, AND DANY DUMONT

Institut des Sciences de la Mer de Rimouski, Université du Québec à Rimouski, Rimouski, Quebec, Canada

(Manuscript received 16 July 2015, in final form 23 December 2015)

ABSTRACT

High-frequency radars (HFRs) measure ocean surface currents remotely through the Bragg scattering of radio waves by surface gravity waves with wavelengths shorter than 50 m. HFR range is affected by sea ice, which dampens surface gravity waves and limits wind fetch for adjacent open waters. HFR range sensitivity to sea ice concentration was empirically determined for two types of HFR—Coastal Ocean Dynamics Applications Radar (CODAR) and Wellen Radar (WERA)—installed on the shores of the lower St. Lawrence estuary, Canada, during winter 2013. One CODAR was operating at 13.5 MHz on the southern shore, and one WERA was operating at 16.15 MHz on the northern shore. Ranges were determined using a signal-to-noise ratio threshold of 6 dB for first-order Bragg scattering measured by the receive antenna elements. Ranges were normalized for expected ranges in ice-free conditions, using empirical relationships determined during summer 2013 between the range and surface gravity wave energy at the Bragg frequencies. Normalized ranges Γ decrease approximately linearly with increasing sea ice concentration C (averaged over the ice-free observational domain) with a slope close to -1 for both HFR types, that is, $\Gamma = 1 - C$. However, for a given sea ice concentration, range can vary significantly depending on the sea ice spatial distribution.

1. Introduction

For more than 30 years, high-frequency radars (HFRs) have been used to map ocean surface currents over wide areas for several practical applications including support for commercial navigation and coastal surveillance (Olascoaga et al. 2006), tracking oil spills (Hodgins 1994) and other toxic materials (Lekien et al. 2005; Coulliette et al. 2007), search and rescue operations (Ullman et al. 2006), and biological research through aiding studying larval dispersal and predicting the population dynamics of commercially exploited species (Bjorkstedt and Roughgarden 1997; Graber and Limouzy-Paris 1997).

High-frequency (HF) remote sensing is based on the scattering of electromagnetic (EM) waves from the rough sea surface, which can be described by the theory

of wave–wave interaction (Bragg scattering; Crombie 1955). HFRs transmit EM waves in the HF band (3–30 MHz), which propagate along the sea surface, and measure the Doppler shift of the backscattered EM waves caused by ocean surface waves and currents. First-order backscattering resonance occurs when the wavelength of the surface waves is one-half of the transmitted EM wavelength (Fig. 1). Surface gravity waves responsible for the resonant Bragg backscattering of the transmitted EM waves will be called Bragg waves hereinafter. Two or more shore-based HFRs allow mapping ocean surface currents over large coastal areas with a horizontal resolution on the order of 1 km.

The capability of HFRs to measure currents is affected by the presence of sea ice (Fig. 2), which limits the wind fetch for open adjacent waters, hence limiting the development of Bragg waves for a given wind speed and duration (WMO 1998). Furthermore, sea ice quickly dampens Bragg waves, which have short periods of 2–6 s (Squire 2007; Dumont et al. 2011). Despite this, mapping surface currents in partially sea ice–covered waters using HFRs has already been done in the past. A 25-MHz Coastal Ocean Dynamics Applications Radar

Corresponding author address: Emna Kamli, Institut des Sciences de la Mer de Rimouski, Université du Québec à Rimouski, 310 Allée des Ursulines, C.P. 3300, Rimouski QC G5L 3A1, Canada.
E-mail: emna.kamli@gmail.com

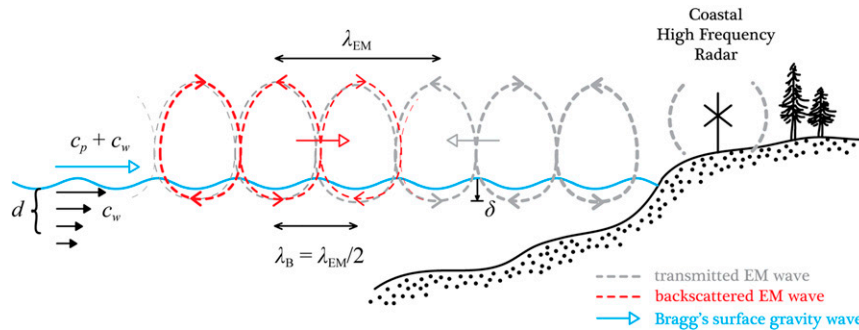


FIG. 1. A schematic showing how HFRs measure surface currents. The HFR emits EM waves that travel in coupled mode along the sea surface via the induction of electrical currents in the conductive seawater. This current induction penetrates only the first few centimeters below the surface (δ). In the presence of surface gravity waves, the EM waves can be backscattered by Bragg waves, i.e., waves having a wavelength λ_B equal to half of the transmitted wavelength λ_{EM} : Since gravity waves propagate at the phase velocity C_p relative to the surface waters, and the latter flow at a velocity C_w relative to the earth, the backscattered signals received by the antennas have a slightly different frequency, due to the Doppler effect. The known wave phase velocity can be subtracted from the total velocity $C_p + C_w$ estimated from the measured Doppler shift to obtain the surface radial component of the surface current C_w . The effective depth of measurement d depends on how surface waves are advected by the vertically sheared near-surface currents.

(CODAR) was deployed in Prudhoe Bay, Alaska, during ice breakup in July 1984 to investigate the possibility of using HFRs to observe ice and water velocities as well as monitoring the ice cover (Lipa et al. 1986). No independent measurement of ice drift or current was collected to validate the HFRs measurements, but they were highly correlated with nearby measurements of wind, encouraging their potential for measuring surface currents or ice drift in winter. Flocco et al. (2003) demonstrated the feasibility of measuring surface currents in the polynya of Terra Nova Bay in the Ross Sea, with shore-based HF radars at 27 MHz. Potter and Weingartner (2010) investigated the performance of shore-based CODARs at 25 and 13 MHz for partially ice-covered waters in the Beaufort Sea. They found that generally ocean currents cannot

be measured in a grid cell containing ice, except for very thin ice or small and isolated ice floes. When a band of ice floes was present between 20 and 30 km offshore with open water near the coast and offshore of the band, radio waves were able to propagate above the band of ice and currents could be measured offshore of the band. However, depending on the speed and direction of the wind, ice-free waters between the coast and the band could limit the fetch for the development of Bragg waves, thus preventing measurement of currents in this area. These interesting results have not yet been published in the refereed literature, and the authors noted that they were unable to investigate the complete parameter space that allows HF radars to measure ocean currents within partially ice-covered waters.

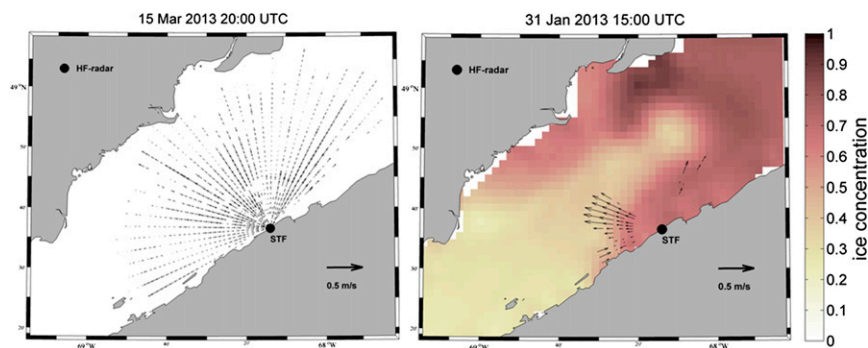


FIG. 2. Current maps obtained from a CODAR HFR at Sainte-Flavie (STF) (Lower St-Lawrence Estuary, Quebec, Canada) in the (right) presence and (left) absence of sea ice. Ice concentration data come from the Canadian operational ice-ocean forecasting system.

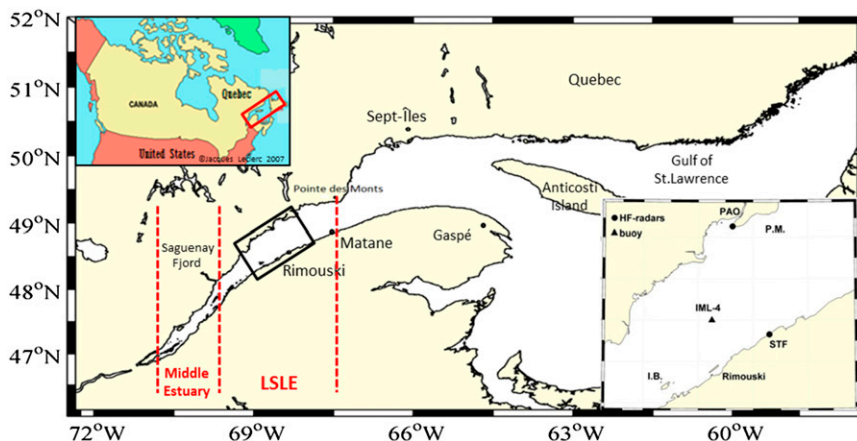


FIG. 3. (bottom-right insert) Study area with the location of HFR and IML-4 buoy. I.B. denotes Bic Islands. P.M. is for Manicouagan Peninsula.

With sea ice coverage and duration decreasing in many polar regions, deployments of HFRs to monitor partially ice-covered waters may increase in the future. It is therefore needed to quantify the impact of sea ice on HFR current measurements.

The aim of this work is to assess experimentally the performance of two types of coastal HF radars, CODAR and Wellen Radar (WERA), to map surface currents in partially ice-covered waters using

different frequencies as a function of ice concentration and wind conditions. The performance of HFR is defined here as the ratio between daily mean ranges achieved by HFR antennas in the presence of sea ice, which will be called R_i , and the estimated daily mean ranges in the absence of sea ice in the same wind conditions, called R_m . Performance is then defined as $\Gamma = R_i/R_m$. Using daily rather than hourly ranges allows for reducing the effect of

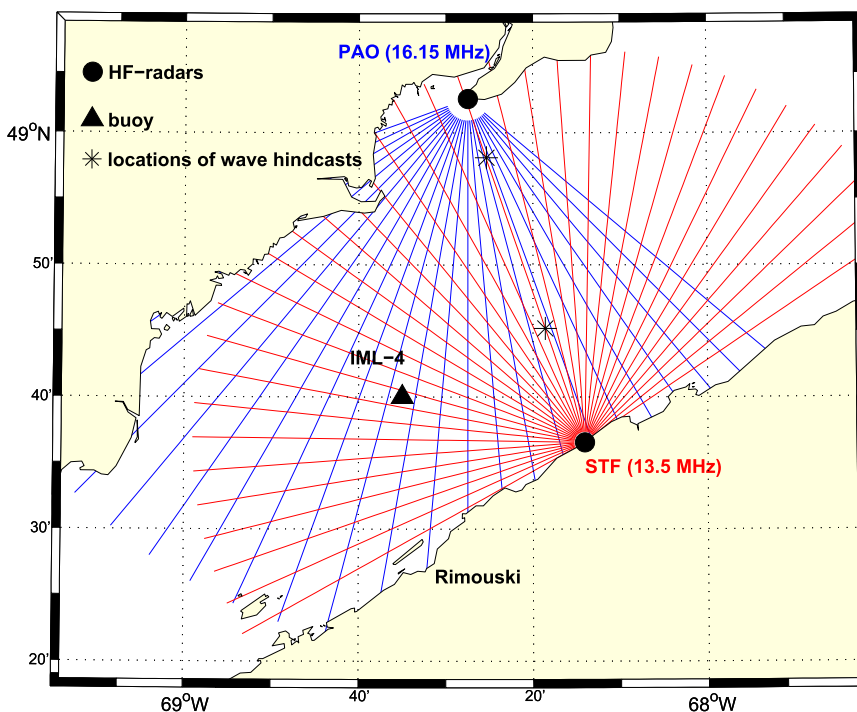


FIG. 4. Map showing the study area and HFR locations with their corresponding polar grids. GENER-predicted waves positions are also indicated.

TABLE 1. HFR characteristics.

	CODAR (STF)	WERA (PAO)
Range resolution (km)	1.5	1.5
Radio frequencies (MHz)	13.5	16.15
Bragg frequencies (Hz)	0.37	0.41
Bragg wavelengths (m)	11.1	9.3

$$R_{\max}^4 = \frac{P_{\text{av}} G_T G_R F \lambda^2 \sigma T_c}{(4\pi)^3 N \alpha L}, \quad (1)$$

ambient electromagnetic noise, which has a characteristic daily cycle.

HFR range depends essentially on the signal-to-noise ratio (α) of the backscattered EM waves and it is given by (e.g., [Headrick and Skolnik 1974](#))

where P_{av} is the average radiated power, G_T is the transmit antenna power gain, G_R is the receiving antenna gain, λ is the radar wavelength, T_c is the coherent processing time, σ is the radar cross section of the water surface within the radar cell, R is the range to radar cell, N is the noise power per unit bandwidth, α is the signal-to-noise ratio, L is for system losses, and F is the factor to account for propagation effects.

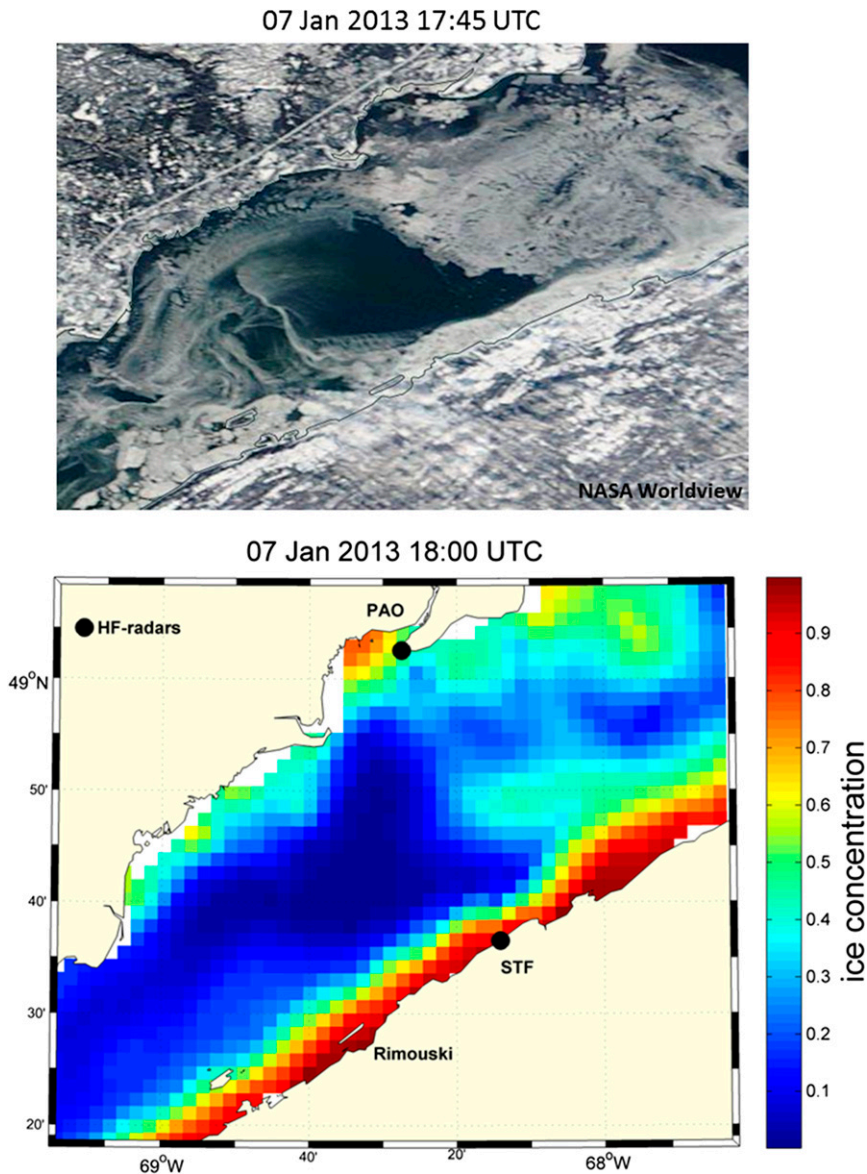


FIG. 5. Comparison between forecasted ice concentration and a MODIS image obtained from NASA Worldview for approximately the same moment of the day.

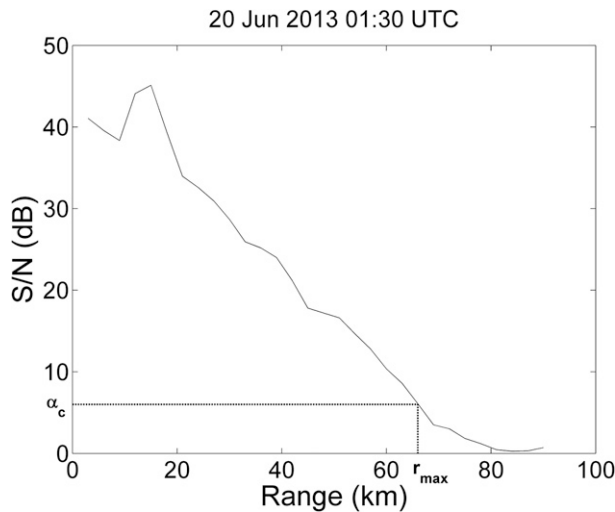


FIG. 6. Example showing the critical value α_c of the signal-to-noise ratio and the corresponding r_{\max} for the receive antenna 10 of the PAO WERA.

In practice, the maximum measurement range is obtained when the SNR reaches a critical value, set here to 6 dB. Performance can therefore be expressed as

$$\Gamma = \frac{R_i}{R_m} = \left(\frac{\sigma_i F_i N_m}{\sigma_m F_m N_i} \right)^{1/4}, \quad (2)$$

assuming system losses L do not change between ice-free and ice conditions.

Performance therefore depends on the radar cross section of water surface within radar cell σ , the propagation factor F , and the noise factor N , which depend on the frequency, salinity, sea ice, sea state, and EM noise (Crombie 1955; Gurgel et al. 1999b; Barrick and Long 2006; Potter and Weingartner 2010).

This paper is organized as follows: the study area, radar system details, and oceanographic and meteorological data sources are described in section 2, which provides also data processing steps applied on HFR and ice data. The results are presented in section 3. The final section summarizes the results and provides a discussion and the conclusions of the study.

2. Data and methodology

a. The study area

The study area is located in the lower St. Lawrence estuary (LSLE; Fig. 3), Canada, characterized by a nonuniform and variable thin ice cover (typically 0.1–0.7 m thick; Saucier et al. 2003) from January to March. Data acquisition was made during the 2012/13 winter, despite the fact this winter represented the sixth lowest ice volume since 1969 (Galbraith et al. 2014).

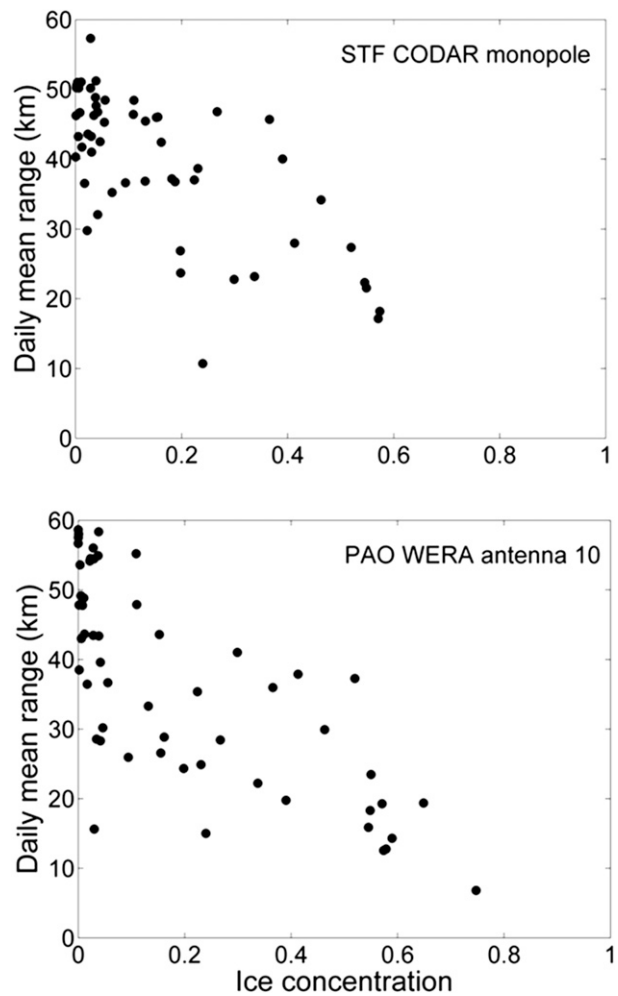


FIG. 7. HFR daily mean ranges vs ice concentration for CODAR and WERA.

The LSLE has a width ranging from 20 to 50 km from the mouth of the Saguenay Fjord to Pointe-des-Monts, Quebec, Canada. It is characterized by an estuarine circulation with the presence of at least two water layers having different physical characteristics: a deep (>150 m) salty layer coming from the northwestern Atlantic with a salinity of 33–35 psu and a temperature of 3°–5°C, and a fresher surface layer affected by the watershed runoff with a salinity of 20–31 psu and a temperature of –1.9° to 14°C (Ingram and El-Sabh 1990). The wave height and period gradually decrease from downstream to upstream of the LSLE due to the decreasing wind fetch. Waves generally observed in the LSLE are produced locally by winds blowing predominantly from the west, while storm waves are generated by northeasterly winds that blow over much longer fetches. The tide is predominantly semidiurnal and its amplitude increases from downstream, where it is

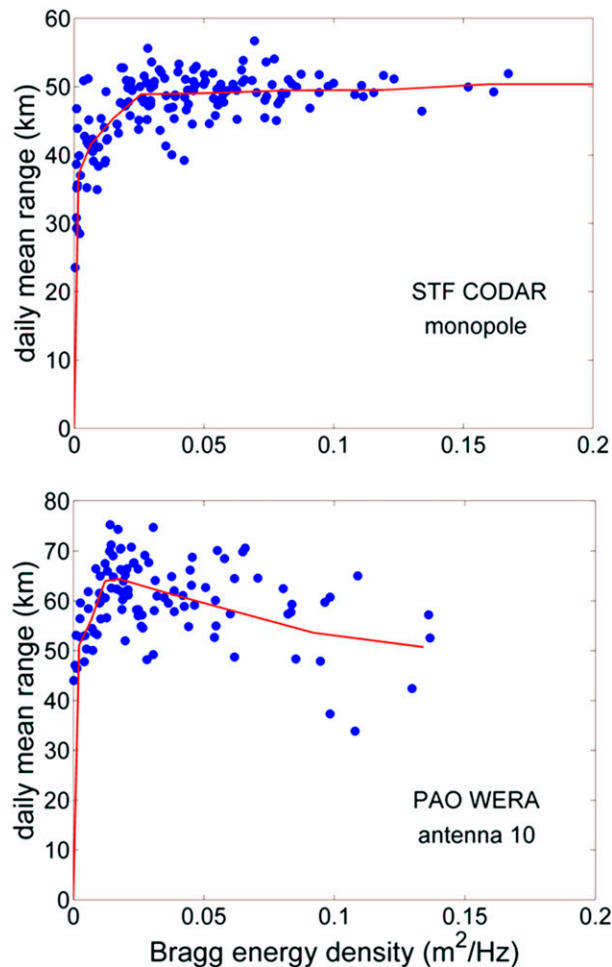


FIG. 8. Daily mean ranges vs Bragg energy density for CODAR and WERA antennas.

about 4.2 m at Pointe-des-Monts (Drapeau 1992), to upstream.

The LSLE is a well-suited natural laboratory to conduct the study, since it is usually partially ice covered from December to March and is easily accessible for HFR installation and maintenance. Furthermore, most environmental parameters affecting HFR performance are observed or forecasted at high spatial and temporal resolutions. In addition, there is a surface oceanographic buoy moored in the radars' field of view [IML-4 buoy operated by the L'Institut Maurice-Lamontagne [Maurice Lamontagne Institute (IML)]; Fig. 3} during ice-free conditions (May–October) that measures waves and winds.

Barrick and Long (2006) showed that EM waves are affected by sea surface salinity only over a depth given by their Eq. (3). A numerical calculation for our HFRs gives a depth of 15 cm for a salinity of 25 psu (\approx surface salinity of the LSLE). Since we have no salinity

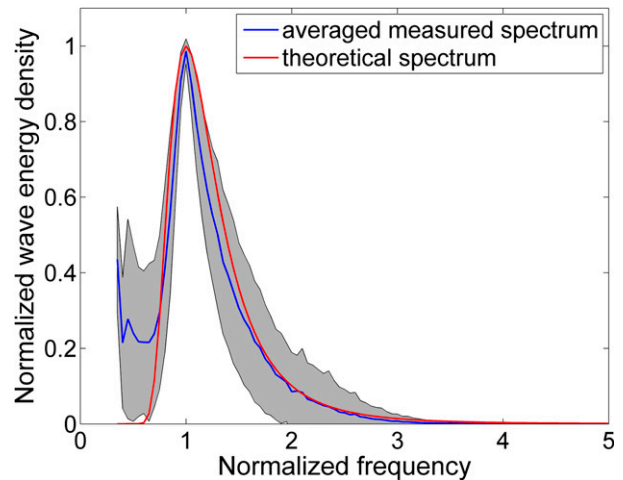


FIG. 9. Comparison between the averaged measured spectrum (blue) and the theoretical spectrum of Bretschneider (red). The standard deviation of the measured spectrum is shown in light gray.

measurements as close to the surface and the LSLE is strongly stratified in salinity, especially near the surface, we cannot quantify the effect of salinity on the radars coverage.

b. HFRs

One CODAR was deployed in November 2012 on the south shore of the LSLE with a frequency of 13.5 MHz at Sainte-Flavie, Quebec (STF; 48.61°N, 68.23°W). On the north shore, one WERA with Northern Radar Inc. antennas was deployed at Pointe-aux-Outardes, Quebec (PAO; 49.04°N, 68.46°W), with 16.15-MHz frequency (Fig. 4). Measurements were taken over 10-min periods. The transmitted chirp bandwidth for all sites is 100 kHz, yielding a range resolution of 1.5 km. The characteristics of each HFR are summarized in Table 1.

c. Oceanographic and meteorological data

Oceanographic and meteorological data used in this study come from numerical models and a surface met-ocean buoy moored near the center of the LSLE. Hourly ice concentrations were obtained from the Canadian operational ice–ocean forecasting system (Smith et al. 2012) through the St. Lawrence Global Observatory (OGSL) web portal, while winds come from the Canadian Global Environmental Multiscale Model (GEM) weather forecasting system (Côté et al. 1998). To check the model skill, we compared its prediction with satellite imagery obtained from NASA Worldview website showing the spatial distribution of sea ice in the study area for a randomly selected image (Fig. 5). Although the image reveals a complex distribution of sea ice at scales not resolved by the model, the general pattern of

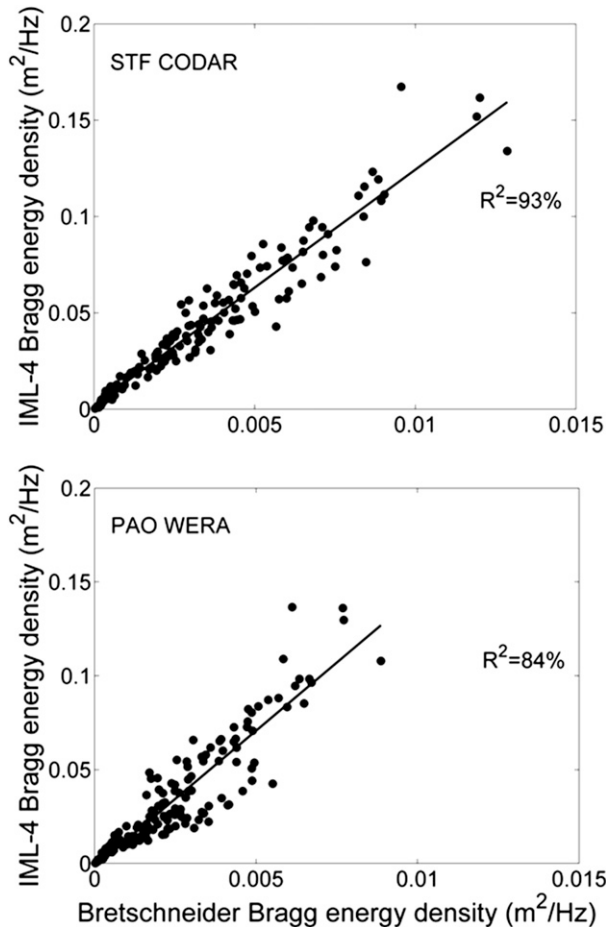


FIG. 10. Observed Bragg energy densities from IML-4 buoy vs estimated Bragg energy densities from the theoretical two-parameter wave Bretschneider's spectrum, with R^2 , for Bragg frequencies corresponding to each HFR.

distribution is relatively well predicted, as the system assimilates RADARSAT ice analyses produced by the Canadian Ice Service.

A parametric wave model called GENER was forced by GEM winds to estimate significant wave heights and peak periods in the LSLE. GENER was developed to predict wind waves at one deep-water location using 2D wind fields and the computed effective fetches for 16 directional sectors around the point of interest (Desjardins and Ouellet 1984; Ruest et al. 2013). The IML-4 buoy (Fig. 4) measured waves and winds during summer from May to October 2013.

d. Data processing

Since CODARs and phased-array WERAs use different techniques for estimating radial currents (direction finding and beam forming, respectively), HFR ranges were determined using the α of receive antennas.

Term α has been calculated for each receive antenna for the WERA and for the three components of the receive antenna for the CODAR HFR. Then, for a critical value of α ($\alpha_c = 6$ dB), the corresponding range achieved by each antenna (r_{\max}) is determined and daily averaged to obtain R_i . Figure 6 shows an example of r_{\max} determination from one raw data file of the PAO WERA for receive antenna 10. Similar results are obtained for the other receive antennas. For simplicity, for the rest, we show results only for the monopole element of the CODAR receive antenna and for antenna 10 of the WERA HFR.

3. Results

a. HFR range versus ice concentration

Hourly ice concentration forecasts were daily and spatially averaged over the domain shown in Fig. 4 (between 48.3° – 49.15° N and 67.7° – 69.25° W). Figure 7 shows R_i versus daily sea ice concentration.

The daily mean range for CODAR and WERA decreases with increasing sea ice concentration. However, since the HFRs operate at different frequencies, other environmental parameters such as wind must be taken into account before their sensitivities to sea ice concentration can be compared.

b. Effect of wind and waves on HFR performance

1) BRAGG ENERGY DENSITY FROM MEASURED WAVE SPECTRA

The Bragg energy density is the gravity wave energy density at the Bragg frequency of the HFR. It has, in principle, a direct effect on HFR measurements by affecting the power of the backscatter radar signal [affecting the radar cross section σ in Eq. (1)].

Raw data of vertical accelerations recorded at the IML-4 buoy at 4 Hz every 10 min have been used to calculate wave spectra (it is assumed that the accelerations of the buoy are only associated with the movement of the waves). The wave spectra were daily averaged over the period from May to October 2013, and then linearly interpolated at the HFR Bragg frequencies (Table 1) to obtain Bragg energy densities. Figure 8 shows HFR daily mean ranges versus daily Bragg energy densities. For both radars, the range decreases when the Bragg energy density approaches $0 \text{ m}^2 \text{ Hz}^{-1}$. For the CODAR the range saturates at 50 km for large Bragg energy densities, whereas it reaches 70–80 km at intermediate Bragg energy values and decreases slightly for larger values for the WERA. Therefore, it is necessary to take these relationships into account before

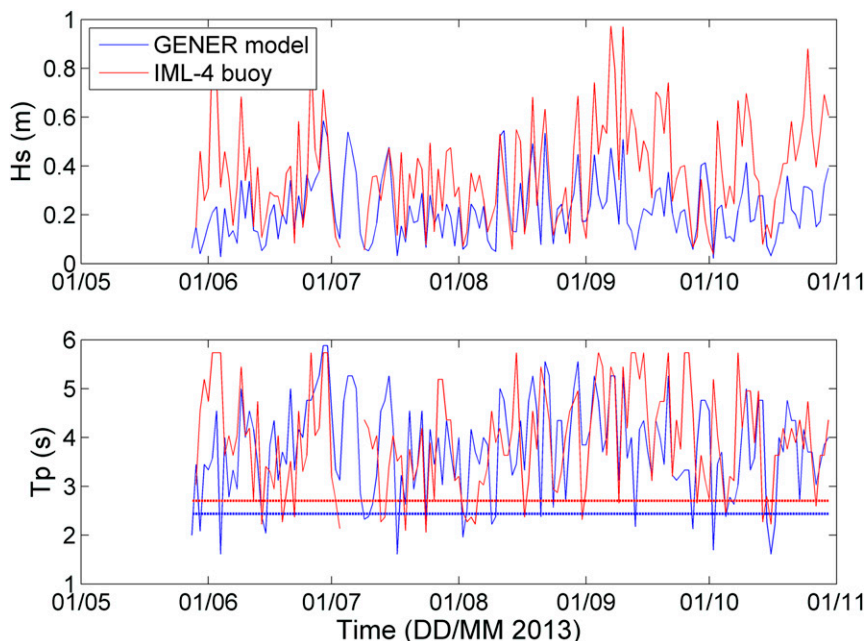


FIG. 11. Comparison between predicted (blue) and measured (red) (top) significant wave heights and (bottom) peak periods, with HFRs Bragg periods shown with dotted lines (STF: red, PAO: blue).

investigating the effect of sea ice. First, HFR daily mean ranges in ice-free conditions can be estimated from Bragg energy densities. To do so, HFR daily mean ranges in ice-free conditions have been empirically fitted to Bragg energy densities by averaging ranges within Bragg energy density bins (the red curve in Fig. 8). Then these averaged daily mean ranges have been interpolated to the Bragg energy densities in winter in order to obtain the estimated daily mean ranges R_m .

2) TWO-PARAMETER BRETSCHNEIDER'S WAVE SPECTRUM

Since wave observations are not available in winter, we investigated whether a theoretical wave spectrum built with significant wave height and peak periods estimates obtained from a parametric fetch model could be used to predict Bragg energy density in winter.

Waves in the LSLE are mostly fetch limited. For example, waves cannot be fully developed for daily winds exceeding 8 m s^{-1} , the wind speed for which waves are limited by the longest fetch of about 300 km (WMO 1998). The Bretschneider spectrum (Bretschneider 1959) is therefore a reasonable choice considering this aspect. This spectrum requires two parameters: the modal frequency (the frequency with maximum energy) and the significant wave height. These two parameters were computed from the wave spectra measured at the IML-4 buoy during summer 2013. The two-parameter

wave Bretschneider's spectrum is defined by the following relation (Ochi 1998, p. 36):

$$S(\omega) = \frac{1,25}{4} \left(\frac{\omega_m^4}{\omega^5} \right) H_s^2 e^{-1,25(\omega_m/\omega)^4}, \quad (3)$$

where H_s is the significant wave height (m), ω is the angular wave frequency (rad s^{-1}), and ω_m is the modal angular frequency (rad s^{-1}).

Daily-averaged measured spectra were normalized by the maximum energy density for periods shorter than 6 s (to avoid swells), and frequencies were normalized by the corresponding peak frequency. These normalized spectra were averaged during the whole observational period (May–October 2013). The resulting average measured spectrum is very similar to the normalized Bretschneider's spectrum (Fig. 9), except at low frequencies.

To check whether the Bretschneider's spectrum could be used in winter to estimate Bragg energy densities, we computed H_s and ω_m from daily-averaged measured spectra in summer and used Eq. (3) to estimate Bragg energy densities. Figure 10 shows the Bragg energy densities from IML-4 spectra versus the Bragg energy densities inferred from the Bretschneider's spectrum built with H_s and ω_m measured by the same buoy. The high correlation coefficients ($R^2 \geq 84\%$) obtained confirm that the Bretschneider spectrum can be used to estimate Bragg energy densities.

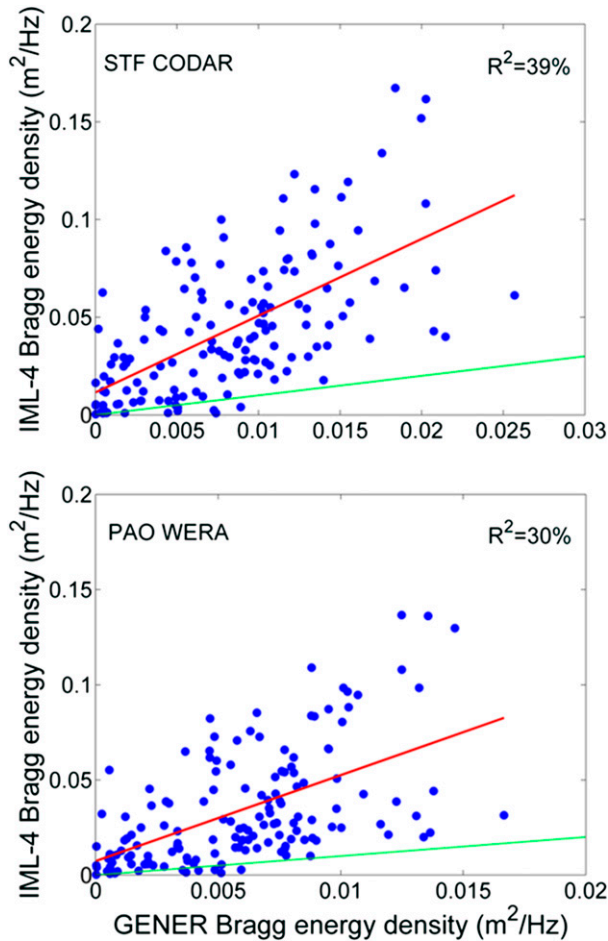


FIG. 12. Observed vs predicted Bragg energy densities for CODAR and WERA. Fitted linear relationships are shown in red and the 1:1 lines are shown in green.

c. GENSER predictions

To separate the effects of wind and sea ice on HFR coverage, we need predictions of waves in the absence of sea ice during winter 2013. Since operational wave forecasting systems parameterize the effect of sea ice on waves, we used a simple fetch model called GENSER (Desjardins and Ouellet 1984; Ruest et al. 2013, 2016).

Wind speed predicted by GEM of Environment and Climate Change Canada has been used to force GENSER during winter 2013 at two positions, each in the corresponding polar grid of the HFR coverage: (48.75°N, 68.31°W) for STF and (48.97°N, 68.42°W) for PAO (stars in Fig. 4). Waves predicted by GENSER are very similar at the two positions (not shown), confirming that using a single position for each HFR is sufficient to represent wave conditions over the entire observational area.

To validate GENSER predictions, we compare daily-averaged predicted (from the GENSER model) and

TABLE 2. Correction coefficients to apply to Bragg energy densities predicted by GENSER (k) [Eq. (4)] and reduction coefficients (b) relating HFR performance to the ice concentration [Eq. (5)] for the two HFRs.

	CODAR (STF)	WERA (PAO)
k	3.9	4.5
b	-0.95	-1

measured (from the IML-4 buoy) significant wave heights ($\langle H_s \rangle_{\text{model}}$ vs $\langle H_s \rangle_{\text{obs}}$) and peak periods ($\langle T_p \rangle_{\text{model}}$ vs $\langle T_p \rangle_{\text{obs}}$) (Fig. 11). Wave spectra measured every 10 min at the buoy were daily averaged and $\langle H_s \rangle_{\text{obs}}$ and $\langle T_p \rangle_{\text{obs}}$ were estimated using the first moment and the peak frequency of the daily-averaged spectra, respectively. Since GENSER predicts H_s and T_p every hour, for consistency with the averaging procedure of the buoy measurements, hourly Bretschneider spectra were computed using the predicted H_s and T_p . Then, the daily-averaged $\langle H_s \rangle_{\text{model}}$ and $\langle T_p \rangle_{\text{model}}$ were estimated from daily-averaged spectra.

Significant wave heights predicted by GENSER underestimate the observed heights but the temporal variability is similar. Peak periods have a similar range, but the temporal variability is less well predicted by GENSER than for significant wave heights. However, these wave parameters are not directly used to estimate the HFRs ranges in ice-free conditions. We therefore computed Bragg energy densities from the daily-averaged spectra predicted by GENSER using the theoretical Bretschneider spectrum and compared them with measured daily-averaged data (Fig. 12). GENSER underestimates measured Bragg energy densities, so linear relationships were least squares fitted ($R^2 \geq 30\%$) to obtain the correction coefficients (Table 2) to apply to GENSER-predicted Bragg energy density in winter:

$$S_{\text{obs}} = kS_p, \tag{4}$$

where S_{obs} is the observed Bragg energy density, k is the correction coefficient given in Table 2, and S_p is the Bragg energy density predicted by the model GENSER.

d. Normalized ranges versus ice concentration

For both HFR types, CODAR (STF) and WERA (PAO), R_i obtained during winter 2013 were normalized by R_m . Figure 13 shows the performance $\Gamma = R_i/R_m$ versus the daily-averaged concentration of sea ice spatially averaged over the entire observational area shown in Fig. 4. Although the normalization of ranges does not affect dramatically the results (cf. Figs. 7 and 13), it allows for comparing the different HFRs together. The performance Γ sometimes exceeds 1 because the fit used

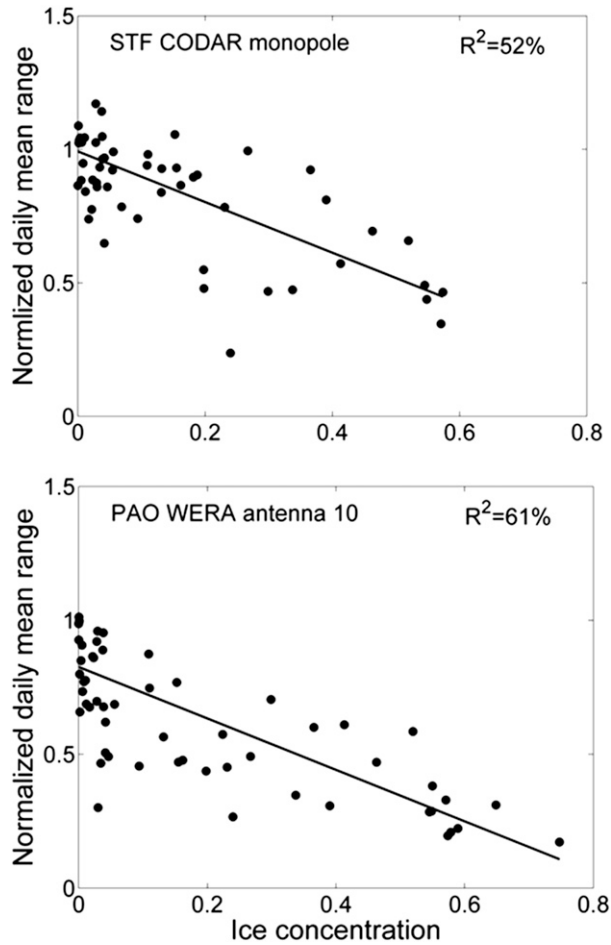


FIG. 13. CODAR and WERA HFR normalized daily mean ranges (Γ) vs ice concentration. Least squares fitted linear relationships are shown by black lines.

to estimate the expected ice-free coverage is a fit to data with a strong scatter (Fig. 8).

A linear relationship was least squares fitted to the data but scatter around the fit is large ($R^2 \leq 61\%$):

$$\Gamma = a + bC, \quad (5)$$

where b is given in Table 2 for the two HFRs. Since b is close to -1 for both HFRs, and given the constraints that $\Gamma = 1$ for $C = 0$ (assuming perfect normalization) and $\Gamma = 0$ for $C = 1$ (no Bragg waves), we propose the following relationship:

$$\Gamma = 1 - C. \quad (6)$$

4. Discussion and summary

The fact that CODAR and WERA were operating at different frequencies, hence required different Bragg

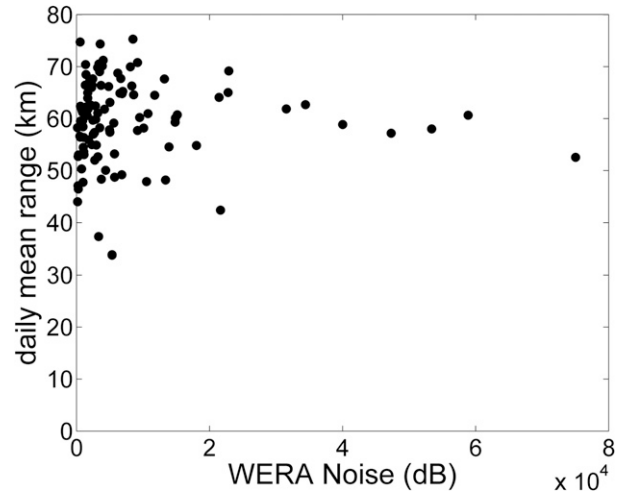


FIG. 14. Daily mean range of the WERA radar vs the ambient radio noise detected by antenna 10.

wavelengths (Table 1), has been taken into account by computing the wave energy at the Bragg frequencies of each radar. We found that both WERA and CODAR antennas were sensitive to the Bragg wave energy density with slightly different relationships (Fig. 8). However, sensitivity to sea ice concentration was similar for both HFR types (Fig. 13). Indeed, backscattering of the signal transmitted by the HF radar is due to the short ocean waves, which are rapidly damped by sea ice, suppressing the constructively interfering return signal. Moreover, the presence of sea ice limits the wind fetch over adjacent open waters, therefore limiting the development of Bragg waves for a given wind speed and duration (WMO 1998). Normalized ranges are sometimes small for CODAR and WERA at low ice concentration and this may be due to the presence of frazil, or landfast ice along the coast in front of the instrument, which was not monitored during this study. Indeed, during winter, ice melts and reforms alternately according to air and sea surface temperature and wind conditions. Before sea ice consolidates and emerges from the water surface as gray-white brash or floes, ice crystals form in the water, which are mixed down to a certain depth (a few tens of centimeters typically) depending on the wave activity. This is called frazil ice and this type of ice does not appear explicitly in ice analyses or in models and is invisible for satellite remote visible or radar sensors. However, frazil can affect the HFR ranges by attenuating ocean waves, decreasing the wave-generation rate by the wind, and modifying the surface salinity. The ice concentration provided by the Canadian operational ice-ocean forecasting system does not represent frazil and neither can we measure it.

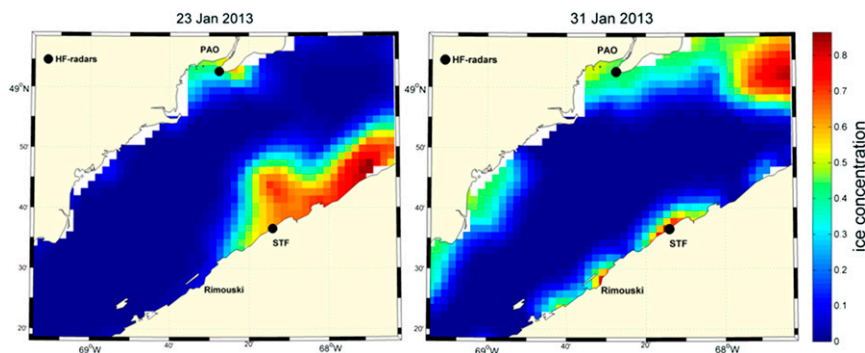


FIG. 15. Ice spatial distribution for similar spatially averaged ice concentration over the study area (≈ 0.2). The average range for the corresponding HFRs is about 38.6 km for STF and 36 km for PAO on 23 Jan 2013 and about 11 km for STF and 12.5 km for PAO on 31 Jan 2013.

The relatively large distribution of the scatters may also be due to uncertainties in our normalization method (large scatter around the relationship between ice-free radar coverage and Bragg energy density, see Fig. 8; uncertainties in GENER Bragg energy density predictions, see Fig. 12), to ambient radio noise variability, and to sea surface salinity variability (Crombie 1955; Potter and Weingartner 2010; Gurgel et al. 1999a; Barrick and Long 2006). Although the noise level was very variable, there is no clear relationship with the HFR range (Fig. 14). Another important factor that can affect the HFR performance is the spatial distribution of sea ice. For example, for approximately the same predicted spatially averaged ice concentration (≈ 0.2), the spatial distribution of sea ice can vary significantly (Fig. 15), and the corresponding HFR average ranges also differ significantly from 23 January 2013 (≈ 38.6 km for STF and ≈ 36 km for PAO) to 31 January 2013 (≈ 11 km for STF and ≈ 12.5 km for PAO). However, taking this into account is beyond the scope of the present study, which focused on obtaining a simple relationship relating HFR ranges to sea ice concentration for future site planning purposes.

Despite the various limitations of our study (predicted rather than observed sea ice concentration, simple parametric wave model to predict expected ice-free Bragg energy densities in winter), it is the first study to quantify experimentally the relationship between HFR ranges and sea ice concentration. Empirical relationships between HFR ranges and environmental parameters (wind and sea ice) will allow for predicting ranges that could be achieved by HFRs installed in other seasonally ice-covered areas.

Acknowledgments. We thank Céline Quentin for the helpful suggestions that improved an earlier version of this work. We acknowledge the University Mission of

Tunisia in Montreal, the FRQNT, the Marine Environmental, Observation, Prediction and Response Network (MEOPAR), Canada Economic Development for Quebec Regions, and Quebec-Ocean for their financial support. We thank Urs Neumeier for producing wave predictions using the GENER model, Simon Senneville and Simon St-Onge Drouin for providing the GEM winds, Fisheries and Oceans Canada for the IML-4 buoy data, and James Caveen for his technical support.

REFERENCES

- Barrick, D. E., and R. Long, 2006: How salinity affects radar performance: A case study of 24 MHz HF radar performance in San Francisco Bay during the 2006 New Year storm floor. CODAR White Paper, 7 pp.
- Bjorkstedt, B. P., and J. Roughgarden, 1997: Larval transport and coastal upwelling: An application of HF radar in ecological research. *Oceanography*, **10** (2), 64–67, doi:10.5670/oceanog.1997.25.
- Bretschneider, C. L., 1959: Wave variability and wave spectra for wind-generated gravity waves. U.S. Army Corps of Engineers Tech. Memo. No. 118, 192 pp.
- Côté, J., S. Gravel, A. Méthot, A. Patoine, M. Roch, and A. Staniforth, 1998: The operational CMC-MRB Global Environmental Multiscale (GEM) model. Part I: Design considerations and formulation. *Mon. Wea. Rev.*, **126**, 1373–1395, doi:10.1175/1520-0493(1998)126<1373:TOCMGE>2.0.CO;2.
- Coulliette, C., F. Lekien, J. D. Paduan, G. Haller, and J. E. Marsden, 2007: Optimal pollution mitigation in Monterey Bay based on coastal radar data and nonlinear dynamics. *Environ. Sci. Technol.*, **41**, 6562–6572, doi:10.1021/es0630691.
- Crombie, D. D., 1955: Doppler spectrum of sea echo at 13.56 Mc/s. *Nature*, **175**, 681–682, doi:10.1038/175681a0.
- Desjardins, L., and Y. Ouellet, 1984: Modèles numériques utilisés pour la conception des ouvrages maritimes. *Comptes rendus du Colloque sur la simulation numérique appliquée au domaine de la ressource hydrique: Dans le cadre du 52e congrès annuel de l'ACFAS*, Université Laval, 187–224.
- Drapeau, G., 1992: Dynamique sédimentaire des littoraux de l'estuaire du Saint-Laurent. *Geogr. Phys. Quat.*, **46**, 233–242, doi:10.7202/032907ar.

- Dumont, D., A. Kohout, and L. Bertino, 2011: A wave-based model for the marginal ice zone including a floe breaking parameterization. *J. Geophys. Res.*, **116**, C04001, doi:10.1029/2010JC006682.
- Flocco, D., P. Falco, P. Wadhams, and G. Spezie, 2003: Surface current measurements in Terra Nova Bay by HF radar. *Antarct. Sci.*, **15**, 55–62, doi:10.1017/S0954102003001147.
- Galbraith, P. S., and Coauthors, 2014: Physical oceanographic conditions in the Gulf of St. Lawrence in 2013. Fisheries and Oceans Canada Doc. 2014/062, vi + 84 pp.
- Grabner, H. C., and C. B. Limouzy-Paris, 1997: Transport patterns of tropical reef fish larvae by spin-off eddies in the Straits of Florida. *Oceanography*, **10** (2), 68–71, doi:10.5670/oceanog.1997.26.
- Gurgel, K.-W., G. Antonischki, H.-H. Essen, and T. Schlick, 1999a: Wellen Radar (WERA): A new ground-wave HF radar for ocean remote sensing. *Coastal Eng.*, **37**, 219–234, doi:10.1016/S0378-3839(99)00027-7.
- , H.-H. Essen, and S. P. Kingsley, 1999b: HF radars: Physical limitations and recent developments. *Coastal Eng.*, **37**, 201–218, doi:10.1016/S0378-3839(99)00026-5.
- Headrick, J. M., and M. I. Skolnik, 1974: Over-the-Horizon radar in the HF band. *Proc. IEEE*, **62**, 664–673, doi:10.1109/PROC.1974.9506.
- Hodgins, D. O., 1994: Remote sensing of ocean surface currents with the SeaSonde HF radar. *Spill Sci. Technol. Bull.*, **1**, 109–129, doi:10.1016/1353-2561(94)90020-5.
- Ingram, R. G., and M. I. El-Sabh, 1990: Fronts and mesoscale features in the St Lawrence estuary. *Oceanography of a Large-Scale Estuarine System*, M. I. El-Sabh and N. Silverberg, Eds., Coastal and Estuarine Studies, Vol. 39, Amer. Geophys. Union, 71–93, doi:10.1002/9781118663783.ch4.
- Lekien, F., C. Coulliette, A. J. Mariano, E. H. Ryan, L. K. Shay, G. Haller, and J. Marsden, 2005: Pollution release tied to invariant manifolds: A case study for the coast of Florida. *Physica D*, **210**, 1–20, doi:10.1016/j.physd.2005.06.023.
- Lipa, B. J., R. D. Crissman, and D. E. Barrick, 1986: HF radar observations of Arctic pack-ice breakup. *IEEE J. Oceanic Eng.*, **11**, 270–275, doi:10.1109/JOE.1986.1145160.
- Ochi, M. K., 1998: *Ocean Waves: The Stochastic Approach*. Cambridge Ocean Technology Series, Vol. 6, Cambridge University Press, 332 pp.
- Olascoaga, M. J., I. I. Rypina, M. G. Brown, F. J. Beron-Vera, H. Koak, L. E. Brand, G. R. Halliwell, and L. K. Shay, 2006: Persistent transport barrier on the West Florida Shelf. *Geophys. Res. Lett.*, **33**, L22603, doi:10.1029/2006GL027800.
- Potter, R. A., and T. J. Weingartner, 2010: Surface circulation radar mapping in Alaskan coastal waters: Beaufort Sea and Cook Inlet. University of Alaska Fairbanks Rep. OCS Study MMS 2009-049, 144 pp.
- Ruest, B., U. Neumeier, D. Dumont, and A. Lambert, 2013: Wave climate evaluation in the Gulf of St. Lawrence with a parametric wave model. *Extended Abstracts of Coastal Dynamics 2013: Coastal Dynamics Research Emphasizing Practical Applications*, P. Bonneton and T. Garlan, Eds., SHOM, 1363–1374. [Available online at http://www.coastaldynamics2013.fr/pdf_files/132_Ruest_Benoit.pdf.]
- , —, —, E. Bismuth, S. Senneville, and J. Caveen, 2016: Recent wave climate and expected future changes in the seasonally ice-infested waters of the Gulf of St. Lawrence, Canada. *Climate Dyn.*, **46**, 449–466, doi:10.1007/s00382-015-2592-3.
- Saucier, F. J., F. Roy, D. Gilbert, P. Pellerin, and H. Ritchie, 2003: Modeling the formation and circulation processes of water masses and sea ice in the Gulf of St. Lawrence, Canada. *J. Geophys. Res.*, **108**, 3269, doi:10.1029/2000JC000686.
- Smith, G. C., F. Roy, and B. Brasnett, 2012: Evaluation of an operational ice–ocean analysis and forecasting system for the Gulf of St. Lawrence. *Quart. J. Roy. Meteor. Soc.*, **139**, 419–433, doi:10.1002/qj.1982.
- Squire, V. A., 2007: Review of ocean waves and sea-ice revisited. *Cold Reg. Sci. Technol.*, **49**, 110–133, doi:10.1016/j.coldregions.2007.04.007.
- Ullman, D. S., J. O'Donnell, J. Kohut, T. Fake, and A. Allen, 2006: Trajectory prediction using HF radar surface currents: Monte Carlo simulations of prediction uncertainties. *J. Geophys. Res.*, **111**, C12005, doi:10.1029/2006JC003715.
- WMO, 1998: Guide to wave analysis and forecasting. 2nd ed. WMO-702, 159 pp.